Research Article

Statistical Real-time Model for Performance Prediction of Ship Detection from Microsatellite Electro-Optical Imagers

Fabian D. Lapierre, Alexander Borghgraef, and Marijke Vandewal

CISS Department, Royal Military Academy, Avenue de la Renaissance, 30, 1000 Brussels, Belgium

Correspondence should be addressed to Fabian D. Lapierre, fabian.lapierre@rma.ac.be

For locating maritime vessels longer than 45 meters, such vessels are required to set up an Automatic Identification System (AIS) used by vessel traffic services. However, when a boat is shutting down its AIS, there are no means to detect it in open sea. In this paper, we use Electro-Optical (EO) imagers for noncooperative vessel detection when the AIS is not operational. As compared to radar sensors, EO sensors have lower cost, lower payload, and better computational processing load. EO sensors are mounted on LEO microsatellites. We propose a real-time statistical methodology to estimate sensor Receiver Operating Characteristic (ROC) curves. It does not require the computation of the entire image received at the sensor. We then illustrate the use of this methodology to design a simple simulator that can help sensor manufacturers in optimizing the design of EO sensors for maritime applications.

1. Introduction

Since a couple of years, the number of illegal acts for taking control of maritime vessels has increased. For search-and-rescue reasons, it is suitable to find efficient sensor systems for detecting vessels. Vessel candidates for illegal acts are often commercial vessels with great dimensions. Such vessels (and all vessels with length greater than 45 m) are required to set up an Automatic Identification System (AIS) used by vessel traffic services for identifying and locating vessels. However, when a ship is shutting down its AIS due to illegal acts or material defects, there are no means to detect it in open sea.

Spaceborne sensors are a valuable tool for noncooperative ship detection when the AIS is not operational. Two classes of spaceborne sensors exist: radar and electro-optical (EO) sensors. As compared to radar sensors, EO sensors have lower cost, lower payload, and better computational processing load. To have a high revisiting time, a constellation of LEO micro-satellites is used. Micro-satellites limit the sensor payload to a few kilograms. Currently, EO sensors are then the best candidate for spaceborne applications. To have day-night capabilities, infrared (IR) sensors are used.

Optimum design of such sensors implies to be capable of simulating the evolution of sensor performance as a function of sensor or scene parameters before manufacturing the sensor. Sensor performance is often expressed using Receiver Operating Characteristic (ROC) curves representing the evolution of the probability of detection with respect to the probability of false alarms. So far, these curves are computed using results of detection algorithms applied to the image received by the sensor. This implies the simulation of these images and the choice of detection algorithms. For our application, since the payload is very limited, the Ground Sampling Distance (GSD) is large (about 100 m). Hence, ship detection cannot solely be pixel-based. This indeed leads to an important rate of false alarms. One possible solution is to detect wakes behind the ship. At large GSD, the turbulent wake is the most visible. It appears bright in optical images (Figure 1) and dark in long-wave IR (LWIR) images (Figure 2). Computing the evolution of ROC curves with sensor or scene parameters is then computationally intensive.

This paper proposes a methodology having real-time capabilities for helping sensor manufacturers in optimizing the design of new EO sensors for maritime (ship detection) applications. This implies to be able to test, in real-time,

FIGURE 1: Example panchromatic (optical) SPOT image of moving ships. Source: [2]. Turbulent wake appears bright.
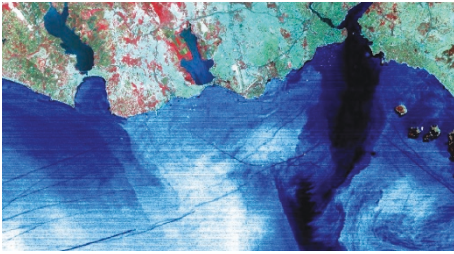

FIGURE 2: Example thermal infrared (LWIR) LANDSAT image of moving ships. Turbulent wake appears dark. Colors correspond to normalized radiance received by the sensor.

the effect of sensor or scene parameters on ROC curves. In IR, near real-time simulators exist [1]. However, they were designed for airborne applications, for which ship detection is done using the contrast between ship and sea background pixels. This cannot be used for spaceborne EO sensors with large GSD. Hence, to our knowledge, there are no real-time tools available for simulating performance of spaceborne EO sensors with large GSD in a maritime environment.

Our approach is based on the one described in [3, 4], where real-time capabilities are obtained by computing ROC curves from a model of the probability density function (pdf) of pixels contained in the image. This avoids simulating the image received by the sensor. In [3, 4], this idea was developed for land-cover scene modeling using hyperspectral sensors. In a maritime environment, a very first attempt to model sea pixels with a pdf was described in [5] for LWIR airborne sensors. To our knowledge, such methodology has not yet been considered for ship detection. This is the subject of the present paper. Our real-time statistical methodology is described in the case of a mid-wave IR (MWIR) sensor. The result is a simple simulator that produces ROC curves in real-time. The proposed statistical methodology can be applied to other EO sensors and even to radar sensors, if appropriate models for the pdfs are used. Such a tool can be very useful for ship detection using Synthetic Aperture Radar (SAR), for which the simulation of SAR images is time consuming [6, 7].

We emphasize that our aim is not to provide a very accurate, validated simulator. Hence, in this paper, performance of the proposed tool is not deeply examined and this tool is not validated using real data. This will be the subject of further research. Our aim is only to propose a real-time methodology for assessing EO sensor performance and to illustrate this methodology by the design of a simple simulator for ship detection using MWIR sensors. Remember that this methodology is inspired from [3, 4].

Section 2 describes the wakes generated behind a moving ship. Section 3 defines ROC curves. Section 4 presents models used for the sea surface and for the turbulent wake. Sections 5 and 6 explain the model of the signal received at the sensor. Section 7 presents the real-time statistical simulator. Section 8 studies its performance. Section 9 concludes.

2. Wakes behind Moving Ships

If a ship is moving, wakes are generated behind it. These wakes are observed for any vessel speed and dimensions and can persist for hours and grow several tens of kilometers long, making it a feature which can easily be detected using spaceborne sensors. It can also provide information on the vessel's heading, speed, and potentially its hull dimensions, which makes it a very desirable feature for detection and tracking purposes. Therefore, wake detection is often used either in combination with or even instead of other ship detection methods.

A ship produces two types of wakes [8]. The turbulent wake, a zone of reduced sea surface roughness which appears as a long bright (optical sensors) or dark (LWIR sensors) streak behind the ship, bounded by a v-wake, and the Kelvin wake, a system of ripples occurring inside a cone of 39 degrees originating at the ship's bow. The Kelvin wake's wave spectrum can be analyzed for determining the ship's speed and heading, and its dimensions. Figure 3 shows a typical wakes pattern.

2.1. Kelvin Wake. The Kelvin wake consists of two systems of ripples, the transverse and divergent waves. These systems [9] are bounded by two cusp-lines separated by an angle of 39 deg. On the cusp-line, a wave propagates with a wavelength λ depending upon the ship speed V: $\lambda = 4\pi V^2/\sqrt{3}g$ with g being the gravity constant.

2.2. Turbulent Wake. The turbulent wake is a zone of high-frequency low-amplitude waves behind the ship's stern. It behaves like a flat but rough surface, therefore contrasting with its surroundings. Hence, the physical quantities of interest are the width and the length of the wake. The turbulent wake's width W depends upon ship dimensions, more specifically its beam (width) B, and its length L. We have

$$W(r) \approx \frac{\overline{w}_0}{(\overline{r}_0 L/B)^{1/\alpha}} B^{\alpha-1} r^{1/\alpha}, \qquad (1)$$

where r is the distance from the ship stern. Here $\overline{r}_0 \approx 4$ and $\overline{w}_0 \approx 4$ are derived from an empiric approximative

formula for the turbulent wake width at four ship lengths. Experimental data show that $\alpha \approx 5$ is a good approximation, though α can vary between 4 and 5. In general, $L/B = 10$ is a good approximation which varies very little for common ship designs [9], resulting in further simplification: $W(r) \approx 1.9 B^{4/5} r^{1/5}$.

The wake length is a more difficult problem and depends upon sea state. The turbulent wake is caused by water displacement due to the ship's hull and propulsion system. This water displacement has a kinetic energy decreasing according to $r^{-4/5}$ [10]. As long as this kinetic energy is significantly larger than the energy of the top water layers, the turbulent wake remains detectable. Typically, turbulent wakes exist during a long period of time. Their length is typically a few kilometers. Figure 4 shows example simulated turbulent wake widths.

3. Definition of ROC Curves

ROC curves are an important signal processing tool for assessing the performance of a sensor or an algorithm. They rely on the definition of a probability density function (pdf) for the signal and the noise [11].

3.1. Signal and Noise Pdfs. In our application, the target signal is the turbulent wake radiance, and the noise signal is the open-sea radiance. Each signal is characterized by a pdf. We thus have two pdfs representing the statistical distribution of the wake signal and of the open-sea signal. They are, respectively, denoted $p_w(S)$ and $p_s(S)$, where S is the level of the signal displayed by the sensor.

3.2. ROC Curves and Detection Algorithm. The detection algorithm works as follows. The value of each pixel in the image received at the sensor is a realization of either $p_w(S)$ or of $p_s(S)$ (or a mix of both pdfs). The mean of each pdf is denoted m_w and m_s, respectively. To perform the detection, we apply a threshold T_{rh} to the pixels in the signal image. If $m_w > m_s$, all pixels greater than T_{rh} are classified as target pixels and other pixels as noise pixels. However, among target pixels, some of them are noise pixels and thus correspond to false alarms. Below, we describe how to evaluate the rate of false alarms.

For a given T_{rh}, we can define a probability of detection $p_d(T_{\mathrm{rh}})$ and a probability of false alarms $p_{\mathrm{fa}}(T_{\mathrm{rh}})$. If $m_w > m_s$, $p_d(T_{\mathrm{rh}})$ and $p_{\mathrm{fa}}(T_{\mathrm{rh}})$ are given by

$$p_d(T_{\mathrm{rh}}) = \int_{T_{\mathrm{rh}}}^{\infty} p_w(S)dS,$$

$$p_{\mathrm{fa}}(T_{\mathrm{rh}}) = \int_{T_{\mathrm{rh}}}^{\infty} p_s(S)dS. \tag{2}$$

Hence, $p_{\mathrm{fa}}(\cdot)$ represents the probability that an open-sea pixel is classified as a wake pixel and $p_d(\cdot)$ represents the probability that a wake pixel is effectively classified as a wake pixel. $p_d(T_{\mathrm{rh}})$ and $p_{\mathrm{fa}}(T_{\mathrm{rh}})$ are represented graphically in Figure 5. Hence, for each T_{rh}, we have one p_d and one p_{fa}. ROC curves are obtained by plotting p_d versus p_{fa} for
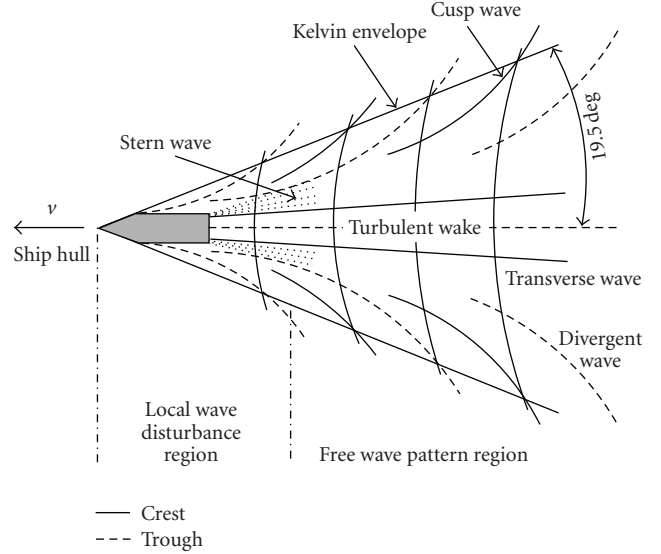

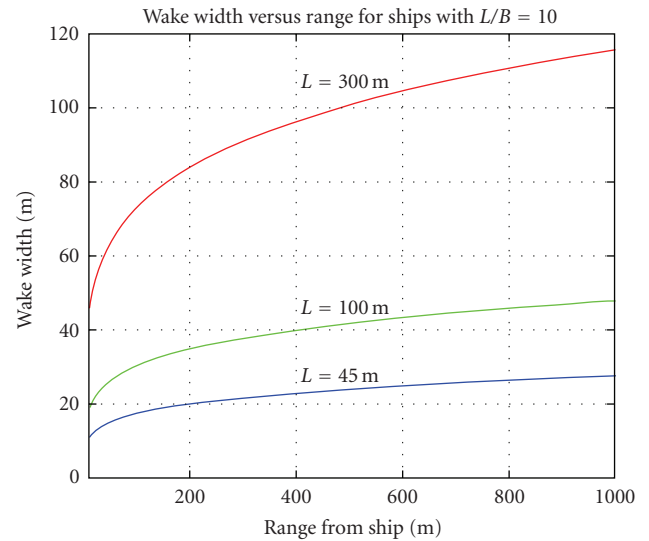FIGURE 3: Different types of wakes appearing behind a moving vessel.

FIGURE 4: Width of the turbulent wake as a function of the distance behind the ship for various ship dimensions.

all possible values of T_{rh}. We can repeat the reasoning if $m_w < m_s$. These curves serve as basis for discussing sensor performance: for a given p_{fa}, p_d should be as high as possible. Below, we describe a model for $p_s(S)$ and $p_w(S)$.

4. Sea and Turbulent Wake Surface Models

Finding $p_s(S)$ and $p_w(S)$ implies to compute the signal received at each pixel in the detector plane of the spaceborne sensor. There are mainly two classes of pixels: open-sea and wake pixels, respectively, containing open-sea and turbulent wake radiances. We first describe how the geometrical
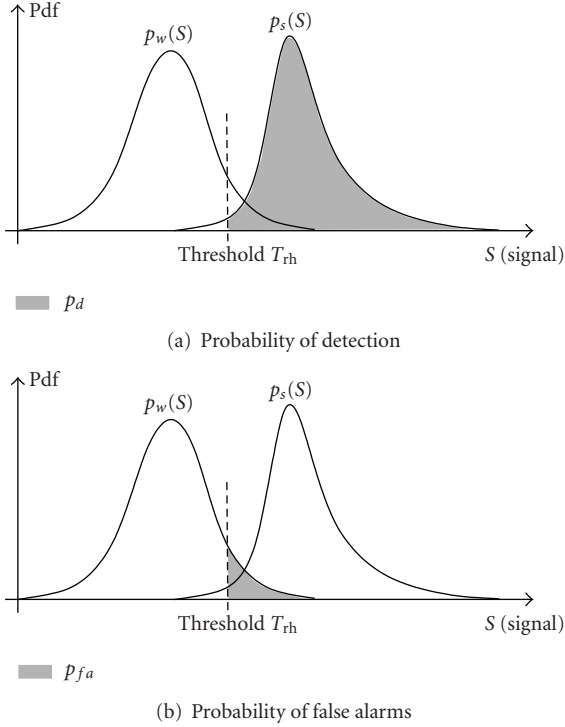
(a) Probability of detection

(b) Probability of false alarms

FIGURE 5: Probability of detection and probability of false alarms.

models of the sea surface and of the turbulent wake surface are obtained.

4.1. Open-Sea Surface Modeling. Our model is based on the model presented in [12, 13]. In realistic sea surface models, we consider three classes of waves: (1) capillarity waves with small wavelength ($\lambda < 5$ cm) influenced by viscosity and surface tension, (2) gravity waves that are wind-driven waves with wavelength $\lambda > 5$ cm and smaller than a few meters, (3) swells being waves with great wavelength, that is, λ is greater than a few meters (these waves originate due to the presence of wind. However, they remain active for a long time after the wind has blown), (4) choppy waves appearing for high wind speed and introducing nonlinearities in the sea surface model (they are the starting point of breaking waves and of the apparition of foam). We only consider gravity waves and swells.

To obtain the sea surface model, we divide the sea surface in small facets. Then, vertical displacements are applied to these facets. These displacements are obtained by modeling the sea surface as a superposition of linear plane waves [14]. A plane wave is given as

$$z(\underline{r}, t) = A e^{j(\omega t + \underline{k} \cdot \underline{r} + \phi)}, \tag{3}$$

where A is the wave amplitude, t is time, $\underline{r} = (x, y)$ is the position vector, ϕ is the phase, and $\underline{k}$ is the wave vector given by $\underline{k} = k(\cos\theta, \sin\theta)$, where $k = 2\pi/\lambda$ is the wave number where λ is the wavelength. θ is the direction of propagation of the plane wave. Gravity waves are modeled as a superposition of a great number of plane waves. Each wave is characterized

by a value for A, k, and ϕ. The wave height $z_w(\underline{r}, t)$ at location $\underline{r}$ and time t is found by integrating the plane waves over the entire space spanned by $\underline{k}$. We thus have

$$z_w(\underline{r}, t) = \int_{\underline{k}} A'(\underline{k}, t) e^{j\underline{k}\cdot\underline{r}} d\underline{k}, \tag{4}$$

where

$$A'(\underline{k}, t) = A(\underline{k}) e^{j(\omega(\underline{k})t + \phi(\underline{k}))}. \tag{5}$$

Hence, $z_w(\underline{r}, t)$ is the inverse Fourier Transform (FT) of $A'(\underline{k}, t)$. Modeling gravity waves is done by specifying a model for $A(\underline{k})$ and for $\phi(\underline{k})$. Modeling swells is done in the same way. The only difference is the model for $A(\underline{k})$ and $\phi(\underline{k})$. For gravity waves, in the case where capillarity waves can be neglected, we have the dispersion relationship [12] $\omega^2(\underline{k}) = gk$, where g is the gravity constant. $\phi(\underline{k})$ is modeled as a random process (RP) that determines the random character of wind-generated waves. Here, $\phi(\underline{k})$ is modeled as a Gaussian RP with zero mean and unit variance. The model of $A(\underline{k})$ depends upon wind speed v and wind direction θ_w. We can write $A(\underline{k})$ as

$$A(\underline{k}) = \sqrt{P(\underline{k}) \cos^2 \Delta\theta}, \tag{6}$$

where $\Delta\theta = \theta - \theta_w$ and $P(\underline{k})$ is the power spectrum often given by the Pierson-Moskowitz spectrum [14], that is,

$$P(\underline{k}) = P(\omega(\underline{k})) = \frac{\alpha g^2}{\omega^5} e^{(-\beta(\omega_0/\omega)^4)}, \tag{7}$$

where $\omega = \sqrt{gk}$, $\alpha = 8.1 10^{-3}$, $\beta = 0.74$, and $\omega_0 = g/v_{19.5}$, where $v_{19.5}$ is the wind speed at 19.5 m above the sea level. There exist other spectra that are tailored to a particular sea [14].

In practice, $z_w(\underline{r}, t)$ in (4) is computed using the 2D inverse FFT (IFFT). Indeed, by discretizing $\underline{k} = (k_x, k_y)$ as $\underline{k}_{m_1 m_2} = (m_1 \Delta k_x, m_2 \Delta k_y)$, where $m_1 \in [0, N_x]$ and $m_2 \in [0, N_y]$ and $\underline{r} = (r_x, r_y)$ as $\underline{r}_{n_1 n_2} = (n_1 \Delta r_x, n_2 \Delta r_y)$, where $n_1 \in [0, N_x]$ and $n_2 \in [0, N_y]$, (4) becomes

$$z_w(\underline{r}_{n_1 n_2}, t) = \sum_{m1,m2} A(\underline{k}_{m_1 m_2}, t) e^{j2\pi(m_1 n_1/N_x + m_2 n_2/N_y)}. \tag{8}$$

The length of the patch where the IFFT is computed is given by $(L_x, L_y) = (N_x \Delta r_x, N_y \Delta r_y)$. The periodicity of the IFFT can be used to replicate the $z_w(\cdot)$'s in both spatial directions. Hence, we can compute sea heights $z_w(\underline{r}, t)$ for extended surfaces at an acceptable computation cost. Figure 6 shows examples of sea surface heights generated with the previous model.

Only considering gravity waves and swells for modeling sea surface is valid for low sea states. For high sea states (typically > 5), breaking waves appear due to gravity. These waves are not handled in this model. The presence of breaking waves only modifies the model for $p_s(S)$; the principles of the method remain unchanged.
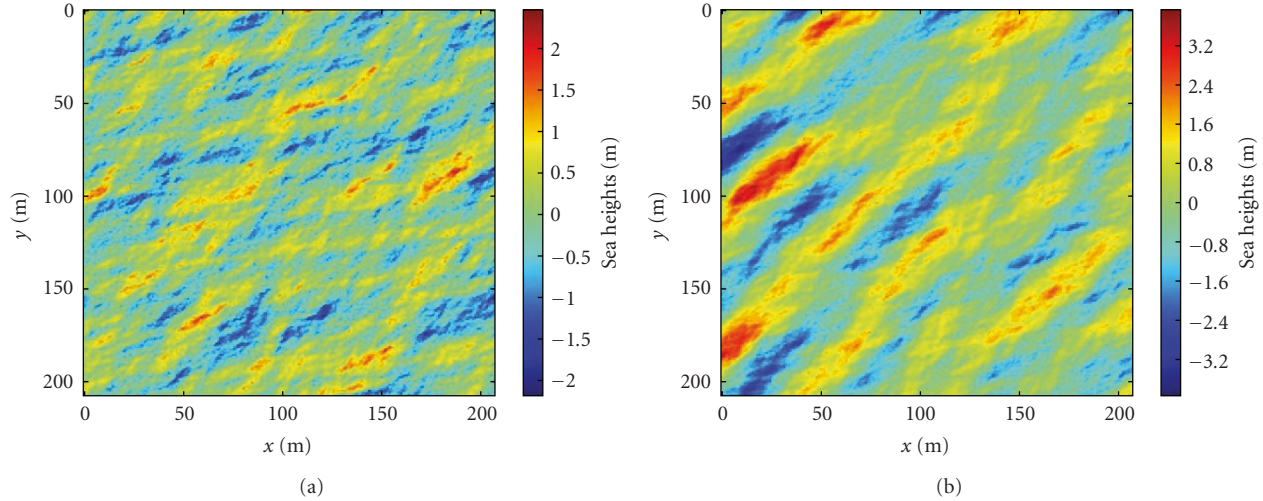
(a)

(b)

FIGURE 6: Examples simulated color-coded sea heights for a wind speed of 11 m/s: (a) gravity waves and (b) gravity waves and swells. x-axis and y-axis are labeled in meters. Color indicates sea heights (in meters). Sea height zero is the mean sea level.

4.2. Turbulent Wake Surface Model. A turbulent wake is modeled as a very rough flat surface [9, 10]. Hence, we model this wake as a flat sea. This flat sea is divided into microfacets (to simulate turbulences), the orientation of these micro-facets being uniformly distributed between 0 and $\pi/2$ to simulate surface roughness.

In Section 5, we see that sea water emissivity (resp., reflectivity) goes down (resp., up) as the angle of arrival of the optical beam on a sea facet increases. Hence, wakes can be distinguished from open-sea thanks to a change in the emissivity (or reflectivity) between wake and open-sea pixels. For optical sensors, the wake appears bright (Figure 1) due to a higher value (higher reflectivity) of the sun glint for wake than for open-sea pixels. For LWIR sensors, the wake appears dark due to a reduction in the emissivity of the sea surface in the wake compared to its value for open-sea pixels. For MWIR sensors, there is a competition between reflection (sun glint and sky irradiance) on sea facets and self-emission of sea facets. This is discussed further below.

5. Radiance Received at the Sensor

Below, we present a model for computing the radiance received at the entry of the sensor. This model can be applied to open-sea and wake pixels.

5.1. Radiance at the Sea Surface (One Sea Facet). We first describe the method for computing the radiance leaving one sea facet n. The radiance $R^n(\lambda)[\text{W/m}^2 \cdot \text{sr}\,\mu\text{m}]$ leaving n for wavelength λ is computed using the following equation [12, 13, 15]:

$$R^n(\lambda) = E_{\text{sea}}^n(\lambda) + E_{\text{sky}}^n(\lambda) + E_{\text{diff}}^n(\lambda) + E_{\text{glint}}^n(\lambda). \quad (9)$$

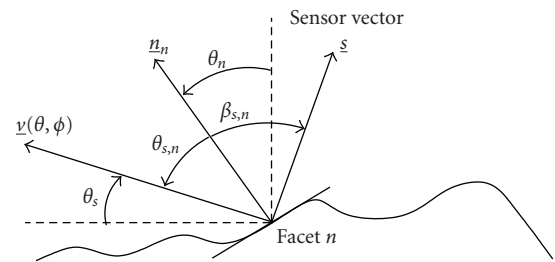We describe below a real-time model for each term in (9). Figure 7 defines useful variables relative to n.

FIGURE 7: Useful variables for a sea facet n.

5.1.1. Emitted Radiance. In (9), E_{sea}^n represents the radiance emitted by n due to its nonzero temperature. It is computed using Planck's law [16], that is,

$$E_{\text{sea}}^n(\lambda) = V_n \varepsilon_{\text{sea}}(\lambda) M_{\text{bb}}(\lambda, T_{\text{sea}}), \quad (10)$$

where $\varepsilon_{\text{sea}}(\lambda)$ is the open sea water emissivity at λ, T_{sea} is the absolute open sea surface temperature, and $M_{\text{bb}}(\cdot)$ is the blackbody radiance [16]. $V_n = 1$ if $\underline{s} \cdot \underline{n}_n > 0$, zero otherwise. The variation of E_{sea}^n with n is mainly due to the variation of $\varepsilon_{\text{sea}}(\lambda)$ with the elevation angle $\beta_{s,n}$ of the optical beam $\underline{s}$ that goes to the sensor. Neglecting the dependence upon wavelength, we have [17]

$$\varepsilon_{\text{sea}}(\lambda, \beta_{s,n}) = 0.98\left(1 - (1 - \cos\beta_{s,n})^5\right). \quad (11)$$

For wake pixels, $\varepsilon_{\text{wake}}(\lambda)$ is the mean of $\varepsilon_{\text{sea}}(\lambda, \beta_{s,n})$ for $\beta_{s,n} \in [0, \pi/2]$. Hence, $\varepsilon_{\text{wake}}(\lambda) = 0.87$. Hence, for wake facets, $\varepsilon_{\text{wake}} < \varepsilon_{\text{sea}}$ for most values of $\beta_{s,n}$.

5.1.2. Sky Radiance. In (9), E_{sky}^n is the irradiance produced by the sky. It is present at any time. There are two models. The first model E_{sky}^n as a blackbody at sky temperature T_{sky} (depending upon weather parameters) [18, 19], that is,

$$E_{\text{sky}}^n(\lambda) = F_n \rho_{\text{sea}}(\lambda, \beta_{s,n}) M_{\text{bb}}(\lambda, T_{\text{sky}}), \quad (12)$$

where $\rho_{\text{sea}}(\lambda, \beta_{s,n}) = 1 - \varepsilon_{\text{sea}}(\lambda, \beta_{s,n})$ is the sea reflectivity and F_n is a visibility factor representing the portion of the sky hemisphere seen by n. This model is realistic under clear-sky conditions. The second model uses MODTRAN [20]. However, it is computationally intensive. To have a real-time model, we use the blackbody model.

5.1.3. Solar Irradiance. The solar extraterrestrial radiation not back-scattered to space reaches the ground in two ways. The radiation reaching the ground directly is the beam irradiance. The scattered radiation reaching the ground is the diffuse irradiance. Below, we assume clear-sky conditions. (For images containing clouds, we assume that cloud masking algorithms [21, 22] have been applied prior to ship detection.) The beam irradiance incident on a surface of 1 m^2 on the earth's ground is

$$E^n_{b,\text{sol}}(\lambda) = E^{n,n}_{b,\text{sol}}(\lambda)\underline{v}(\theta, \phi) \cdot \underline{n}_n = E^{n,n}_{b,\text{sol}}(\lambda) \cos \theta_{s,n}, \quad (13)$$

where

$$E^{n,n}_{b,\text{sol}}(\lambda) = \alpha V_n c(\lambda) M_{\text{sol}}(\lambda), \quad (14)$$

where α is a proportionality constant and $c(\lambda)$ is obtained from MODTRAN and accounts for propagation through the atmosphere. $M_{\text{sol}}(\lambda)$ is the spectral radiance of the sun computed either using a blackbody at $T_{\text{sun}} = 5760$ K or using MODTRAN (more accurate). In (9), $E^n_{\text{glint}}(\lambda)$ corresponds to the reflected beam solar irradiance, that is, the solar glint. Assuming that n is a Lambertian (diffuse) reflector (diffuse solar glint), we have

$$E^n_{\text{glint}}(\lambda) = \rho_{\text{sea}}(\lambda, \beta_{s,n}) E^n_{b,\text{sol}}(\lambda). \quad (15)$$

E^n_{diff} is the diffuse irradiance reflected by n. Since we consider clear-sky conditions, we neglect E^n_{diff} since it is a small fraction of $E^n_{b,\text{sol}}$. To reduce computation time, $E^{n,n}_{b,\text{sol}}$ at all zenith angles are precomputed and the value corresponding to a given zenith angle is obtained by interpolation of the pre-computed $E^{n,n}_{b,\text{sol}}$'s.

5.2. Radiance at Sea Level (One Pixel). The radiance $R^p(\lambda)$ leaving an open-sea pixel corresponding to the IFOV of the sensor is

$$R^p(\lambda) = S_h \sum_n R^n(\lambda) A_n \, [\text{W/ sr} \, \mu\text{m}], \quad (16)$$

where A_n is the area of n and S_h is a shadowing coefficient smaller than one if the satellite is not at zenith. Indeed, in this case, some sea facets are shadowed by other sea facets. Modeling of S_h implies to resort to ray-tracing algorithms (highly time-consuming). Here, we use a simplified, but realistic expression [12], that is,

$$S_h(\nu) = \frac{2}{1 + \text{erf}(\nu) + (1/\nu\sqrt{\pi})e^{-\nu^2}}, \quad (17)$$

where $\text{erf}(\cdot)$ is the error function, $\nu \equiv \tan \theta / \sigma$, where θ is the satellite look angle and σ is the RMS slope of the facets [23], that is, $\sigma^2 = 0.003 + 0.00512 \nu^2_{12.5}$, where $\nu_{12.5}$ is the average wind speed at 12.5 m above sea level.

5.3. Radiance at the Spaceborne Sensor. To obtain the radiance $R^{s,i}$ arriving at the entrance of the spaceborne sensor, we multiply R^p by the solid angle of the sensor (using the radius r_p of the entrance pupil and the satellite height H_s). We obtain

$$R^{s,i}(\lambda) = \frac{\pi r_p^2}{H_s^2} R^p(\lambda) c(\lambda) + L_{\text{path}}(\lambda) \, [\text{W/}\mu\text{m}], \quad (18)$$

where L_{path} represents the radiance received on the path between the sea surface and the sensor and $c(\lambda)$ is the atmospheric transmittance. For MWIR sensors, L_{path} represents the radiance emitted by the atmosphere on the path between n and the sensor. It can then be modeled as the integral of a blackbody with height-dependent temperature. We then approximate L_{path} using a blackbody at a temperature being the mean of the air temperature along the path to the sensor.

6. Signal Displayed by the Sensor

We describe the model for converting $R^{s,i}(\lambda)$ to the signal displayed at each pixel of the sensor.

6.1. Model for the Displayed Signal (No Noise). $R^{s,i}(\lambda)$ is transferred by the sensor optics to the detector focal plane where the image is formed. The spectral irradiance at the entry of a detector located on the optical axis is related to $R^{s,i}(\lambda)$ by the camera equation [15]

$$R^s(\lambda) = \frac{\pi \tau_o(\lambda)}{4N^2} R^{s,i}(\lambda) \, [\text{W/}\mu\text{m}], \quad (19)$$

where $\tau_o(\lambda)$ is the optical system transmittance (often 90% and nearly flat), N is the f-number. Then, the detector converts collected photons in an electrical current [A] (photo-electric effect). The efficiency of this transformation is $a_{qe} \in [0, 1]$. Next, $R^s(\lambda)$ is spectrally filtered by the spectral response $S_b(\lambda)$. The resulting signal R^b is the integration of $R^s(\lambda)$ over the spectral interval $[\lambda_1, \lambda_2]$ corresponding to the bandpass of the detector. To increase the SNR, the signal is temporally integrated over a time interval (integration time) specified by I_τ. Hence,

$$R^b = I_\tau a_{qe} \int_{\lambda_1}^{\lambda_2} S_b(\lambda) R^s(\lambda) d\lambda \cdot [C]. \quad (20)$$

Here, we assume that $\tau_o(\lambda) = \tau_o$ and $S_b(\lambda) = 1$ for all $\lambda \in [\lambda_1, \lambda_2]$. R^b is expressed in Coulomb (C). Dividing R^b by the electrical charge e^- of an electron, we get the number N^b of electrons collected by the detector, that is, $N^b = R^b/e^-$.

If the imaged scene is a point source, the image produced at the detector is a blurred point due to diffraction. The resulting image is called the Point Spread Function (PSF) PSF(x, y). For any other imaged scene, the signal $R^{\text{bl}}(x, y)$ at each pixel (x, y) on the detector plane is given by a convolution of $R^b(x, y)$ with PSF(x, y), that is,

$$R^{\text{bl}}(x, y) = \int_\alpha \int_\beta R^b(\alpha, \beta) \text{PSF}(x - \alpha, y - \beta) d\alpha \, d\beta. \quad (21)$$

For real systems, the PSF also includes nonideal effects. With each effect, a PSF is associated. The global PSF is the convolution of all PSFs. Typical nonidealities are the following. First, the optics induce blurring by the optical PSF as explained above. The image formed by the optics may move during the integration time; this introduces image motion PSF (also called smearing PSF). High-frequency (resp., low frequency) vibrations of the satellite also imply a degradation of the signal. We then associate to these vibrations a jitter (resp., pointing) PSF. The detector also adds additional blurring due to the detector PSF. Finally, the detected signal is further degraded by the electronics PSF.

Computation of (21) is computationally intensive. One alternative is to compute the FT of the PSFs. The convolution becomes a product. The FT of a PSF is called a Modulation Transfer Function (MTF). Hence,

$$R^{\mathrm{bl}}(x, y) = \mathcal{F}^{-1}\Big(\mathrm{MTF}(u, v)\mathcal{F}\big(R^{b}(x, y)\big)\Big), \qquad (22)$$

where $\mathcal{F}(f(x))$ (resp., $\mathcal{F}^{-1}(f(x))$) is the FT (resp., inverse FT) of $f(x)$. In practice, $R^{\mathrm{bl}}(x, y)$ is a discrete function since the number of detectors in the detector plane is finite. $R^{\mathrm{bl}}[i, j]$ represents the current received at detector located at position (i, j). Similarly, $N^{\mathrm{bl}}[i, j] = R^{\mathrm{bl}}[i, j]/e^{-}$ is the number of electrons collected at (i, j).

6.2. Inclusion of Noise.

So far, the proposed model for R^{bl} does not include noise present in the detector. In EO sensors, the most important noise sources are the following: (1) the photon (shot) noise associated with the nonequilibrium conditions in a potential energy barrier of a photovoltaic detector through which a dc current flows; (2) the thermal (Johnson) noise associated to fluctuations in the voltage current caused by the thermal motion of charge carriers in resistive materials, (3) the multiplexer (read out) noise.

Each noise is modeled as a random process (RP) with zero mean and variance σ_{pn}^{2} (photon noise), σ_{tn}^{2} (thermal noise), or σ_{mn}^{2} (multiplexer noise). Models for these variances can be found in [24]. Each noise is expressed in number of electrons. The total detector noise variance σ_{n}^{2} is then the sum of σ_{pn}^{2}, σ_{tn}^{2}, and σ_{mn}^{2}, so that

$$\sigma_{n} = \sqrt{\sigma_{\mathrm{pn}}^{2} + \sigma_{\mathrm{tn}}^{2} + \sigma_{\mathrm{mn}}^{2}}. \qquad (23)$$

There exist two other noise sources (the quantization noise and bit errors) [3]. However, they are not considered here. Notice that these noises only modify the value of σ_{n}; the reasoning remains unchanged. The signal $S^{\mathrm{bl}}[i, j]$ displayed by the sensor at detector $[i, j]$ is then

$$S^{\mathrm{bl}}[i, j] = N^{\mathrm{bl}}[i, j] + N^{n}[i, j], \qquad (24)$$

where $N^{n}[i, j]$ is a realization of the zero-mean Gaussian RP with variance σ_{n}^{2}.

7. Real-Time Simulator

Evaluating sensor performance implies first to simulate $S^{\mathrm{bl}}[i, j]$ for all detectors in the detector plane. This is computationally intensive due to the inclusion of the PSF (or MTF). Hence, evaluating sensor performance using this approach is not possible in real-time. Below, we propose an efficient, real-time strategy.

First, observe that, for an image in the open-sea, we have three classes of pixels: (1) pixels only composed of open-sea radiance, (2) pixels only composed of wake radiance, and (3) mixed pixels composed partially of open-sea radiance and of wake radiance. For each class of pixels, we propose below an RP for the received signal. Hence, instead of simulating the entire image, we only have to find a model for the pdf of the three classes of pixels. Indeed, the entire image is found by considering realizations of these three RPs. To summarize, we propose to reduce the computation of the entire image to the computation of three pdfs, one for each class of pixels. ROC curves are then obtained as discussed in Section 3.

7.1. Probability Density Function for R^b.

We first consider the pdf of an open-sea pixel. Then, we consider a wake pixel and finally, a mixed pixel.

7.1.1. Open-Sea Pdf.

The signal R^{b} corresponding to an open-sea pixel is denoted R_{s}^{b} and is given by (20) using the geometric model of Section 4.1. R_{s}^{b} mainly depends on satellite position $\underline{s}_{s}$, sun location $\underline{v}(\theta, \phi)$, and wind speed v. Consider that $\underline{s}_{s}$, $\underline{v}(\theta, \phi)$, and v are fixed. Consider a great open-sea area divided in small planar facets for which we compute sea heights (see Section 4). We then compute the received R_{s}^{b} for each facet, and we plot the corresponding histogram. This gives an idea of the pdf of R_{s}^{b} for open-sea pixels. Results are shown for various sea states (various wind speeds) in Figure 8 for MWIR sensors. Figure 8 shows normalized R_{s}^{b}'s, denoted as $\widetilde{R}_{s}^{b}$, that is, $\widetilde{R}_{s}^{b} \in [0, 1]$, obtained as

$$\widetilde{R}_{s}^{b} = \frac{R_{s}^{b} - R_{s,\min}^{b}}{R_{s,\max}^{b} - R_{s,\min}^{b}}, \qquad (25)$$

where $R_{s,\min}^{b}$ and $R_{s,\max}^{b}$ are, respectively, the minimum and the maximum values of R_{s}^{b} for all sea facets.

Histograms of $\widetilde{R}_{s}^{b}$ all have the shape of a beta statistical distribution. The pdf $p_{\beta}(r)$ of this distribution has two free parameters θ_{1} and θ_{2} and is given by

$$p_{\beta}\big(\widetilde{R}_{s}^{b}, \theta_{1}, \theta_{2}\big) = \frac{1}{B(\theta_{1}, \theta_{2})}\big(\widetilde{R}_{s}^{b}\big)^{\theta_{1}-1}\big(1 - \widetilde{R}_{s}^{b}\big)^{\theta_{2}-1}, \qquad (26)$$

where $B(\theta_{1}, \theta_{2}) = \Gamma(\theta_{1})\Gamma(\theta_{2})/\Gamma(\theta_{1} + \theta_{2})$, where Γ is the gamma function. To find the $p_{\beta}(\widetilde{R}_{s}^{b}, \theta_{1}, \theta_{2})$ that best fits the $\widetilde{R}_{s}^{b}$'s, we estimate θ_{1} and θ_{2} using the mean m_{r} and the variance σ_{r}^{2} of the $\widetilde{R}_{s}^{b}$'s. We have [25]

$$\hat{\theta}_{1,s} = m_{r}\left(\frac{m_{r}(1 - m_{r})}{\sigma_{r}^{2}} - 1\right), \qquad (27)$$

$$\hat{\theta}_{2,s} = (1 - m_{r})\left(\frac{m_{r}(1 - m_{r})}{\sigma_{r}^{2}} - 1\right). \qquad (28)$$
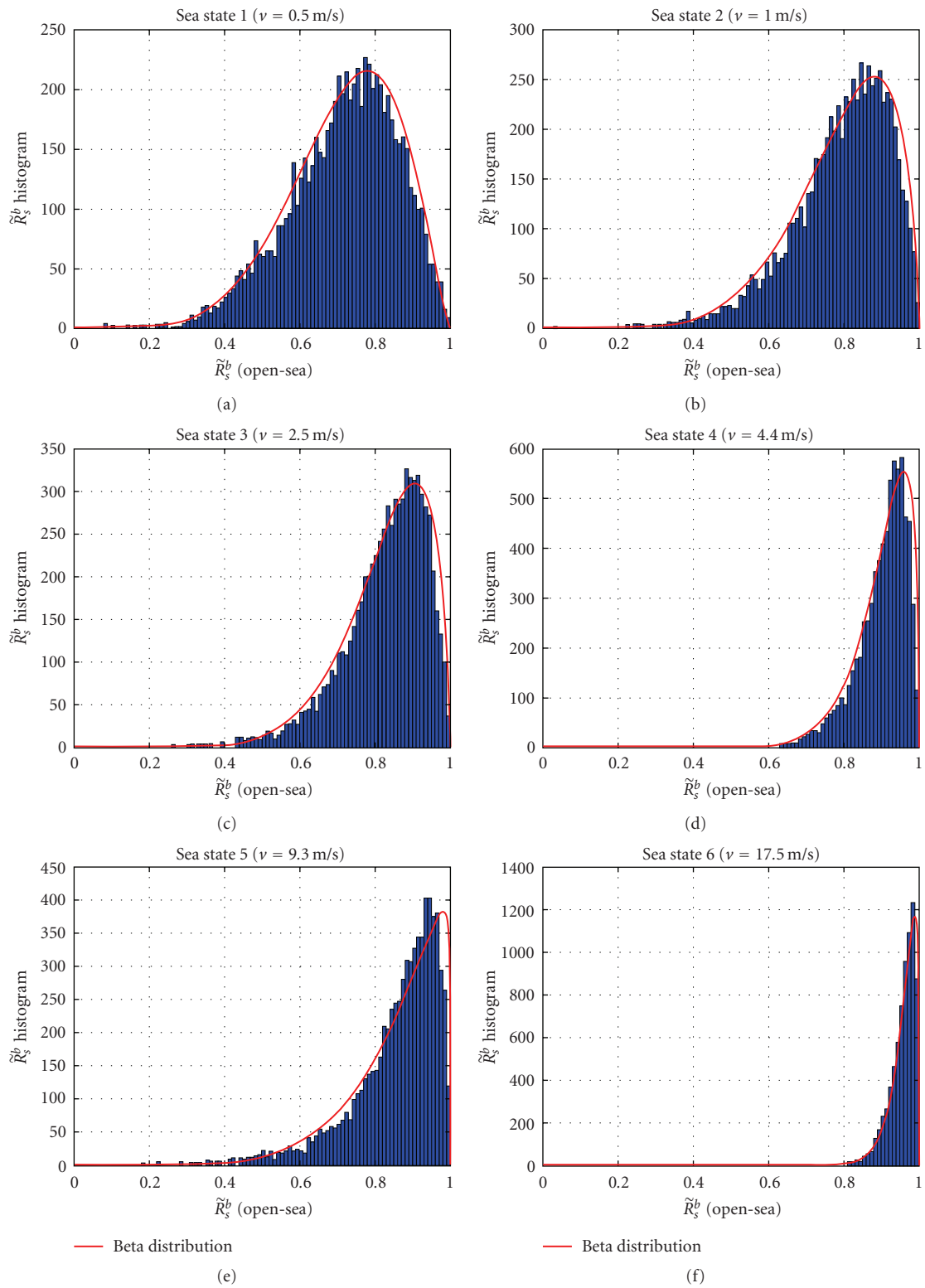
FIGURE 8: Histogram of $\widetilde{R}_s^b$'s and corresponding beta distributions.

Hence, the pdf $p_{s,b}(R_s^b)$ of the R_s^b's is $p_\beta(\tilde{R}_s^b, \theta_1, \theta_2)$, where $\tilde{R}_s^b$ is replaced by R_s^b using (25) and θ_1 and θ_2 are, respectively, replaced by $\hat{\theta}_{1,s}$ and $\hat{\theta}_{2,s}$, that is,

$$p_{s,b}\left(R_s^b\right) = p_\beta\left(\frac{R_s^b - R_{s,\min}^b}{R_{s,\max}^b - R_{s,\min}^b}, \hat{\theta}_{1,s}, \hat{\theta}_{2,s}\right). \qquad (29)$$

The reason why the open-sea R_s^b's can be modeled as a beta distribution is currently not well understood.

7.1.2. Turbulent Wake Pdf. We consider a model for the pdf $p_{w,b}$ of the signal R_w^b corresponding to a wake pixel given by (20) with the geometrical model of Section 4.2. We consider that $\underline{s}_s$, $\underline{v}(\theta, \phi)$, and v are fixed. In Section 4, we saw that R_w^b corresponds to the radiance of a flat sea with important roughness. This roughness is modeled by dividing the wake pixel in microfacets with arbitrary orientation. (For computing R_w^b, we consider that the wake surface temperature T_w is equal to T_{sea}. However, in practice, $T_w < T_{\text{sea}}$[26]. Modeling this temperature difference is outside the scope of this paper.) The simplest model for $p_{w,b}$ thus considers a uniform pdf for the emissivity leading to a uniform distribution of R_w^b. However, this is not realistic since having microfacets with arbitrary orientation is more probable than having microfacets with horizontal orientation. One solution is to use a beta distribution with high probability density near the signal corresponding to microfacets with orientation uniformly distributed between 0 and $\pi/2$ (denoted as R_{wu}^b) and a very small probability density near the signal corresponding to a flat sea (denoted as R_{flat}^b). If $R_{\text{flat}}^b > R_{wu}^b$, we have

$$p_{w,b}\left(R_w^b\right) = p_\beta\left(\frac{R_w^b - R_{wu}^b}{R_{\text{flat}}^b - R_{wu}^b}, \theta_{1,w}, \theta_{2,w}\right), \qquad (30)$$

where $\theta_{1,w}$ and $\theta_{2,w}$ are such that $p_\beta(\varepsilon) \simeq 1$ and $p_\beta(1-\varepsilon) \simeq 0$, with $\varepsilon \ll 1$. Simulations show that $\theta_{1,w} = 1$ and $\theta_{2,w} = 20$ lead to a meaningful pdf. Figure 9 shows $p_{w,b}$.

7.1.3. Mixed Pdf. Some pixels, called mixed pixels and located at the edge of the wake, are composed of a portion of wake and a portion of open-sea (Figure 10). The signal R_m^b corresponding to a mixed pixel is then

$$R_m^b = \alpha R_w^b + (1 - \alpha)R_s^b, \qquad (31)$$

where α is the portion of wake signal in the pixel. We then have to find a model for the pdf $p_{m,b}$ of R_m^b. Computing the analytical expression of the pdf of a linear combination of different beta distributions is challenging. In Section 7.2.3, we propose a method for computing this pdf. We use this method here with weights α and $1 - \alpha$. The resulting pdf is then a beta distribution (see Section 7.2.3) given by

$$p_{m,b}\left(R_m^b\right) = p_\beta\left(\frac{R_m^b - R_{m,\min}^b}{R_{m,\max}^b - R_{m,\min}^b}, \hat{\theta}_{1,m}, \hat{\theta}_{2,m}\right), \qquad (32)$$

where $R_{m,\min}^b$ and $R_{m,\max}^b$ are, respectively, the minimum and the maximum values of R_m^b, obtained using the minimum
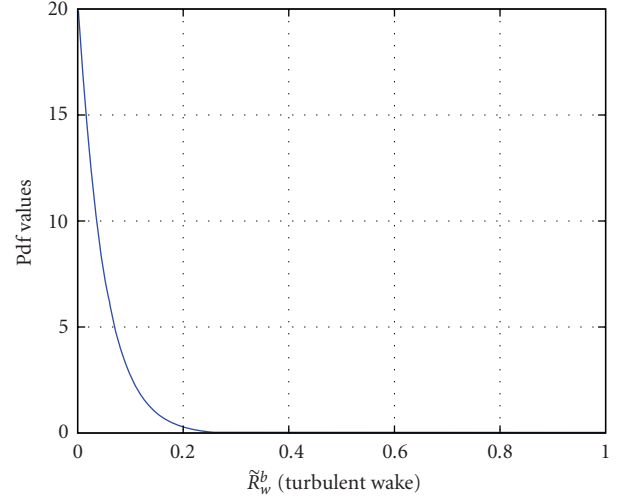

FIGURE 9: Pdf of $\tilde{R}_w^b$: beta distribution with $\theta_{1,w} = 1$ and $\theta_{2,w} = 20$.
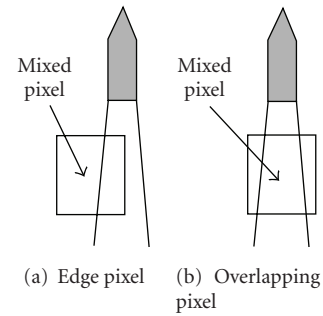

(a) Edge pixel (b) Overlapping pixel

FIGURE 10: Mixed pixels: (a) Edge and (b) overlapping mixed pixels.

and the maximum values of R_s^b and R_w^b. Coefficients $\hat{\theta}_{1,m}$ and $\hat{\theta}_{2,m}$ are obtained as explained in Section 7.2.3. An example of mixed pixel pdf is given in Figure 11.

7.2. Statistical Model for R^{bl}. Below, we describe the model for the pdf p_{bl} of R^{bl} for a mixed pixel. The approach is similar for open-sea and wake pixels. Finding a model for $p_{m,bl}(R_m^{bl})$ implies to include the effect of the PSF. We can either compute the convolution of the PSF with the image pixels or perform the FT of the image and multiply the resulting image by the MTF. Both methods are computationally intensive: they require the computation of the entire image. Below, we propose an efficient method to include the effect of the PSF without computing the entire image.

Moreover, to simulate the effect of changing the PSF (or MTF) of one particular nonideality on sensor performance, we should first be able to easily change the shape of the PSF (or MTF) and second to update ROC curves in real-time. Hence, we propose to represent each PSF (or MTF) with one scalar value: the MTF at Nyquist. This allows to rapidly update sensor performance.
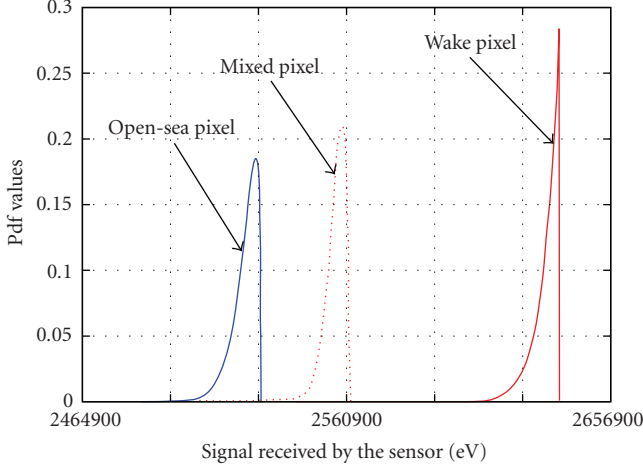
FIGURE 11: Example pdf of a mixed pixel for $\alpha = 0.4$, sea state 5, GSD of 100 m, and wake width of 40 m. Simulation corresponds to sunlight dominating (bright) wake.

7.2.1. MTF at Nyquist. If a sensor is looking at a scene, each detector of the sensor senses a pixel of size equal to the GSD. For a line of detectors, the values received at these detectors correspond to the sampling of a continuous signal corresponding to the radiance produced by all patches on the ground line corresponding to the detector line. Hence, the maximum frequency of the signal that can be sensed is $f = 1/2\text{GSD}$. Signals with higher frequencies produce aliasing. Hence, the MTF MTF_N at Nyquist frequency $f_N = 2f = 1/\text{GSD}$ plays an important role in evaluating sensor performance. f_N is often expressed using the detector size d to be independent upon the GSD. Hence, $\text{MTF}_N = 1/d$. The MTF can then be characterized by one scalar value, that is, MTF_N.

7.2.2. Model for the MTF. Each MTF is then described by its MTF_N. For each nonideality n_i, we have a value of MTF_N, denoted $\text{MTF}_{N,i}$. The global MTF_N is the product of the $\text{MTF}_{N,i}$'s. Sensor designers provide two MTF functions: the along-track and the across-track MTF. Both MTF are combined to give the 2D MTF. We thus have two MTF_N, that is, the along-track MTF_N ($\text{MTF}_{N,\text{al}}$) and the across-track MTF_N ($\text{MTF}_{N,\text{ac}}$). We make the reasonable assumption that the 2D MTF is Gaussian [15]. This allows to compute the inverse FT analytically, saving computation time. Hence,

$$\text{MTF}_G(u,v) = \left(e^{-\pi^2 u^2/a}\right)\left(e^{-\pi^2 v^2/b}\right), \qquad (33)$$

where u and v are normalized frequency variables (with respect to d) and a and b are determined using $\text{MTF}_{N,\text{al}}$ and $\text{MTF}_{N,\text{ac}}$. Estimates $\hat{a}$ and $\hat{b}$ of a and b are $\hat{a} = -\pi^2/\ln(\text{MTF}_{N,\text{al}})$ and $\hat{b} = -\pi^2/\ln(\text{MTF}_{N,\text{ac}})$. $\text{PSF}_G(x,y)$ is the inverse FT of $\text{MTF}_G(u,v)$, which is also a Gaussian, that is,

$$\text{PSF}_G(x,y) = \left(\sqrt{\frac{a}{\pi}}e^{-\hat{b}y^2}\right)\left(\sqrt{\frac{b}{\pi}}e^{-\hat{a}x^2}\right), \qquad (34)$$

where x and y are normalized detector locations (with respect to d). $\text{PSF}_G(x,y)$ is used to compute R_m^{bl} in (21).

7.2.3. Model for R_m^{bl}. Consider a detector (i,j). Hence, discretizing integrals in (21), we obtain

$$R_m^{\text{bl}}[i,j] = \sum_{k\in\mathcal{K}}\sum_{l\in\mathcal{L}} R^b[k,l]\text{PSF}_G(i-k,j-l), \qquad (35)$$

where $\mathcal{K}$ and $\mathcal{L}$ are the sets of pixel indexes centered on (i,j) and for which PSF_G has a nonnegligible value. With typical values of MTF_N, the sizes of $\mathcal{K}$ and $\mathcal{L}$ are about 3 to 4. Hence, R_m^{bl} is evaluated by summing signals of about 9 to 16 pixels, which is very efficient. Now, we describe a model for the pdf $p_{m,\text{bl}}$ of R_m^{bl}. R_m^{bl} in (35) is a weighted sum of RPs. Indeed, each R^b in (35) is the signal corresponding either to an open-sea pixel or to a wake pixel or to a mixed pixel that all are RPs. Hence, we can compute mean $m_{\text{bl}}[i,j]$ and variance $\sigma_{\text{bl}}^2[i,j]$ of $R_m^{\text{bl}}[i,j]$. We have

$$m_{\text{bl}}[i,j] = \sum_{k\in\mathcal{K}}\sum_{l\in\mathcal{L}} m_b[k,l]\text{PSF}_G(i-k,j-l), \qquad (36)$$

where $m_b[k,l]$ is the mean of $R^b[k,l]$. For $\sigma_{\text{bl}}^2[i,j]$, we have

$$\sigma_{\text{bl}}^2[i,j] = \sum_{k\in\mathcal{K}}\sum_{l\in\mathcal{L}} \sigma_b^2[k,l]\text{PSF}_G^2(i-k,j-l), \qquad (37)$$

where $\sigma_b^2[k,l]$ is the variance of $R^b[k,l]$. Using $m_{bl}[i,j]$ and $\sigma_{\text{bl}}^2[i,j]$, we can model $p_{m,\text{bl}}$ as a beta distribution with parameters $\hat{\theta}_{1,\text{bl}}$ and $\hat{\theta}_{2,\text{bl}}$, respectively, given by (27) and (28), where m_r and σ_r^2 are, respectively, replaced by $m_{\text{bl}}[i,j]$ and $\sigma_{\text{bl}}^2[i,j]$. Hence, $p_{m,\text{bl}}$ is

$$p_{m,\text{bl}}\left(R_m^{\text{bl}}\right) = p_\beta\left(\frac{R_m^{\text{bl}} - R_{m,\text{min}}^{\text{bl}}}{R_{m,\text{max}}^{\text{bl}} - R_{m,\text{min}}^{\text{bl}}}, \hat{\theta}_{1,\text{bl}}, \hat{\theta}_{2,\text{bl}}\right), \qquad (38)$$

where $R_{m,\text{min}}^{\text{bl}}$ and $R_{m,\text{max}}^{\text{bl}}$ are the minimum and the maximum values of R_m^{bl}, obtained using the minimum and maximum values of each $R^b[k,l]$ with $k\in\mathcal{K}$ and $l\in\mathcal{L}$.

Figure 12 compares (a) $p_{s,b}$ and $p_{m,b}$ (Figure 12(a)) $p_{s,\text{bl}}$ and $p_{m,\text{bl}}$ (Figure 12(b)). We first conclude that $p_{s,\text{bl}}$ and $p_{m,\text{bl}}$ are close to a Gaussian distribution. This is a consequence of the Central Limit Theorem. Second, the separation between $p_{s,\text{bl}}$ and $p_{m,\text{bl}}$ is smaller than the one between $p_{s,b}$ and $p_{m,b}$ indicating that the MTF degrades detection performance.

7.3. Statistical Model for Signal S^{bl}. We propose a model for the pdf of S^{bl} for the three classes of pixels. Since the method is similar for these three classes, we only consider a mixed pixel, that is, S_m^{bl}. S_m^{bl} for detector $[i,j]$ is given by (24) where N_m^{bl} is modeled as a beta distribution with parameters $\hat{\theta}_{1,\text{bl}}$ and $\hat{\theta}_{2,\text{bl}}$ and where N^n is modeled as a zero-mean Gaussian RP with variance σ_n^2. The pdf $p_{m,s}(S)$ of the RP S_m^{bl} is then the sum of a beta distribution and a Gaussian pdf. The mean m_s and the variance σ_s^2 of S_m^{bl} are, respectively, given by (36) and (37), that is,

$$\begin{aligned} m_s &= m_{\text{bl}}, \\ \sigma_s^2 &= \sigma_{\text{bl}}^2 + \sigma_n^2, \end{aligned} \qquad (39)$$

where m_{bl} and σ_{bl}^2 are the mean and the variance of N_m^{bl}. Using m_s and σ_s^2, we can model $p_{m,s}(S)$ as a beta distribution with parameters $\hat{\theta}_1$ and $\hat{\theta}_2$, respectively, given by (27) and (28), where m_r and σ_r^2 are, respectively, replaced by m_s and σ_s^2. Hence, $p_{m,s}(S)$ is

$$p_{m,s}(S) = p_\beta\left(\frac{S - S_{m,\min}}{S_{m,\max} - S_{m,\min}}, \hat{\theta}_1, \hat{\theta}_2\right), \quad (40)$$

where $S_{m,\min} \simeq N_{m,\min}^{bl}$ and $S_{m,\max} \simeq N_{m,\max}^{bl}$.

7.4. Line Detection Algorithms.

Since we consider low payload sensors, the spatial resolution is small. Hence, the IR ship-only signature is spread between a small number of pixels. Using pixel-based ship detection algorithms thus gives high p_{fa}. A ship pixel is indeed easily confused with open-sea pixels with sun glint or open-sea pixels corresponding to swells or cloud pixels. (For ship detection, we assume that cloud masking algorithms have been applied prior to detection [21, 22].) We then have to use more than one pixel for ship detection. Below, we investigate how to detect ships using their turbulent wake. Indeed, this wake can persist a few kilometers away from the ship, making their detection with low-resolution sensors possible. The wake appears either as a curved or a straight line (Figures 1 and 2). Curve tracing and curve detection algorithms can then be used to detect and separate wakes [27, 28], reducing p_{fa}.

Since we want to develop a real-time methodology for evaluating sensor performance, computing the entire image and the corresponding curve detection algorithms is time consuming. Below, we propose a statistical, real-time approach. We describe the algorithm principles in the case of a straight line. The methodology is easily generalized to curved wakes. Consider a ship moving in a given direction and the corresponding wake. A line is then visible in the image. Consider the application of a line-detection algorithm to the center pixel of the ship. There are an infinite number of lines passing through this pixel. These lines generate a curve in the line-space. Each point on this curve is weighted by the percentage of the length of the line in the original image that effectively crosses a line in the original image. Hence, this curve exhibits a maximum when the line is confounded with the wake.

Instead of thresholding the contrast between two pixels, we threshold the contrast between two lines of pixels; the first line is the wake (or a mix between the wake and an open-sea line) and the second line is an open-sea line. Hence, if we are able to compute the pdf $p_s^{L,N}$ of the signal of a line of N open-sea pixels and the pdf $p_w^{L,N}$ of the signal of a line of N wake (or mixed) pixels, we can compute ROC curves after the application of line-detection algorithms. Below, we explain how to compute the pdf $p_m^{L,N}(S)$ of the signal of a line of N mixed pixels. The same method is used to compute $p_s^{L,N}(S)$ and $p_w^{L,N}(S)$.

Consider N mixed pixels. Each pixel is an RP described with the same pdf $p_{m,s}(S)$. One realization of the RP of the line is obtained by performing the mean between N realizations of the RP with pdf $p_{m,s}(S)$. Hence, using (36) and (37), the mean $m_{L,N}$ and the variance $\sigma_{L,N}^2$ of the line RP are
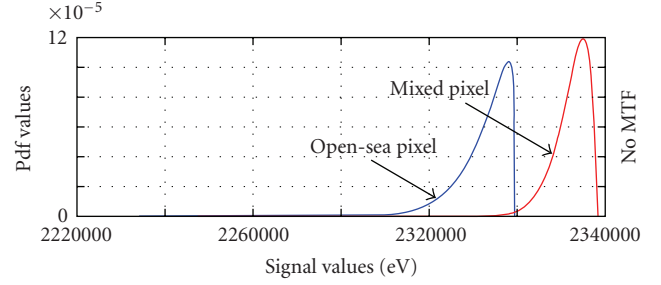
(a)
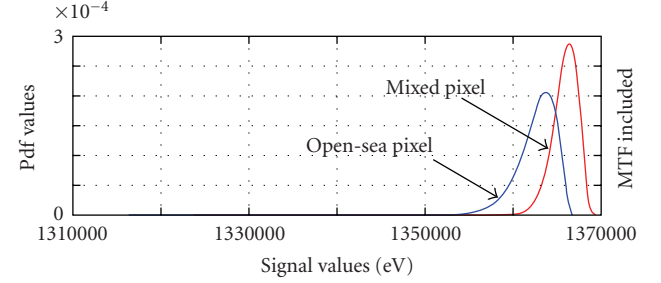
(b)

FIGURE 12: Comparison between (a) $p_{s,b}$ and $p_{m,b}$ and (b) $p_{s,bl}$ and $p_{m,bl}$ for sea state 5 and $\alpha = 0.4$. Simulation corresponds to sunlight dominating (bright) wake.
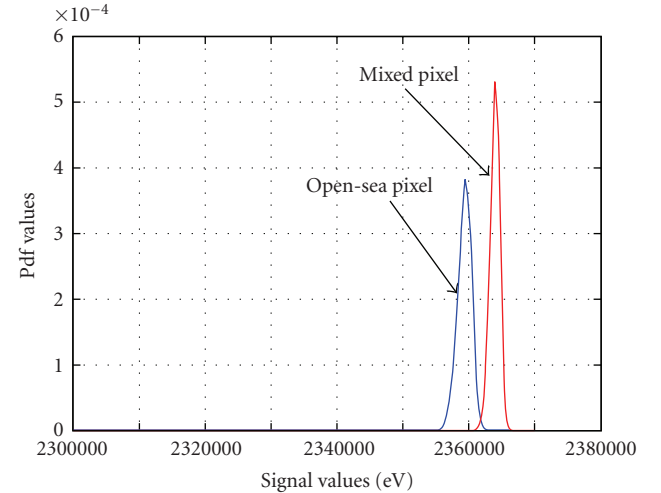

FIGURE 13: Pdfs $p_s^{L,N}$ and $p_m^{L,N}$ for sea state 5 and $N = 10$. Simulation corresponds to sunlight dominating (bright) wake.

given by $m_{L,N} = m_{m,s}$ and $\sigma_{L,N}^2 = \sigma_{m,s}^2/N$, where $m_{m,s}$ and $\sigma_{m,s}^2$ are, respectively, the mean and the variance of $p_{m,s}(S)$. Using (27) and (28), we, respectively, obtain estimates $\hat{\theta}_{1,L}$ and $\hat{\theta}_{2,L}$ of the parameters θ_1 and θ_2 of the resulting beta distribution. Hence,

$$p_m^{L,N}(S) = p_\beta\left(\frac{S - S_{m,\min}}{S_{m,\max} - S_{m,\min}}, \hat{\theta}_{1,L}, \hat{\theta}_{2,L}\right). \quad (41)$$

Figure 13 shows $p_s^{L,N}$ and $p_m^{L,N}$ for $N = 10$. We first conclude that $p_s^{L,N}$ and $p_m^{L,N}$ are close to a Gaussian distribution.

TABLE 1: Value of all parameters for the MWIR scenario.

MWIR sensor	Value
GSD (m)	100
# pixels	1024×1024
pixel size (μm)	15
FOV (°)	9.8×9.8
Swath (km)	102×102
Integration time (ms)	10
Focal length (mm)	90
Entrance pupil (mm)	30
Transmittance τ_o	0.6
Average QE	0.75

This is a consequence of the Central Limit Theorem. Second, the separation between $p_s^{L,N}$ and $p_m^{L,N}$ is greater than the one between $p_{s,bl}$ and $p_{m,bl}$ (see Figure 12(b)) illustrating that the line-detection algorithm enhances detection performance.

8. Performances

In this section, we illustrate the use of the presented simulator to assess sensor performance using ROC curves. The set of simulations is chosen as broad as possible in order to show that this simulator can be used in realistic scenarios. Remember that our aim is not to present validation results of the simulator. We consider the scenario of Table 1 with the MTF$_N$'s and the noise variances of Table 2.

We first illustrate ROC curves for three cases: (a) no MTF (Figure 14(a)), (b) MTF included (Figures 14(b) and 14(c)) line detection + MTF (Figure 14(c)). We see the degradation of performance due to the inclusion of the MTF. The ROC curve for line detection shows the important gain obtained with such algorithms. In practice, performance is more degraded due to the presence of nondiffuse sun glint that increases p_{fa}.

Second, Figures 15(a) and 15(b), respectively, show the evolution of sensor performance for different wake widths and different satellite look angles. This illustrates the fact that sensor performance degrades as wake width decreases and as satellite looks at the sea with an angle closer to the horizontal direction. We assume that the sensor FOV is small enough so that each pixel sees the sensor with the same angle. These results were obtained in real-time.

Next, we consider the difference between day and night conditions. During the night, sun glint is absent. Figure 16(a) compares sea, wake, and mixed pixels pdfs. For MWIR sensors, there is a competition between reflections on the sea surface (reflection of the sun and the sky irradiances) and self-emission of the sea surface facets [15]. During the day, due to the presence of sun glint, reflections dominate over self-emission and then the wake appears bright (the wake pdf is located at the right of the open-sea pdf). During the night, the absence of sun glint reduces the importance of reflections and self-emission dominates. Then, the wake appears dark
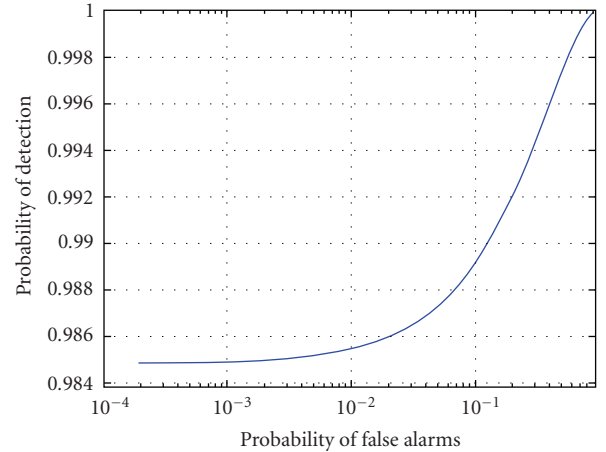
(a) No MTF
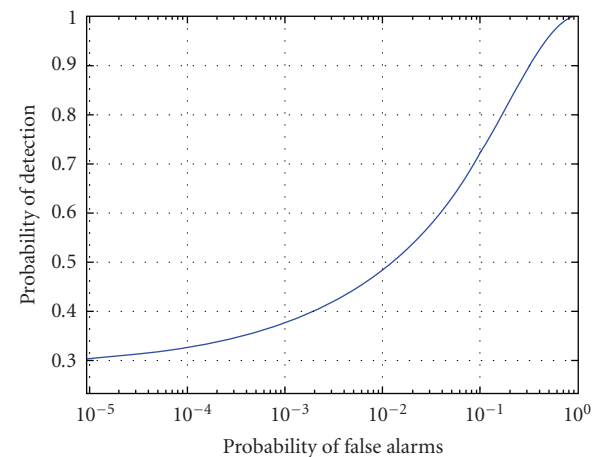
(b) MTF included
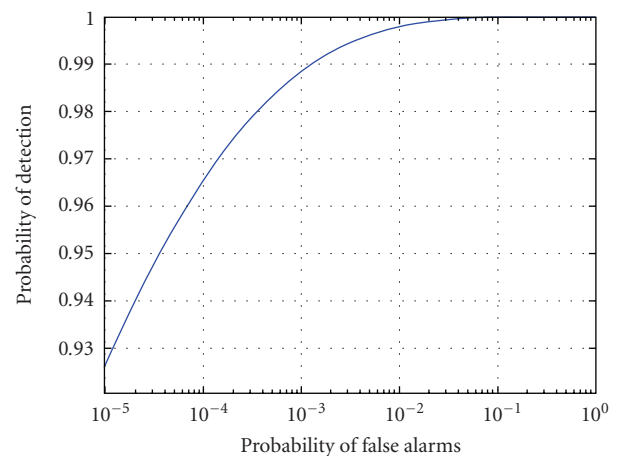
(c) MTF and line detection included

FIGURE 14: ROC curves for scenario of Tables 1 and 2 (wake width of 40 m and sea state 5). (a) MTF not included in the model, (b) MTF included, and (c) MTF and line detection algorithm included.
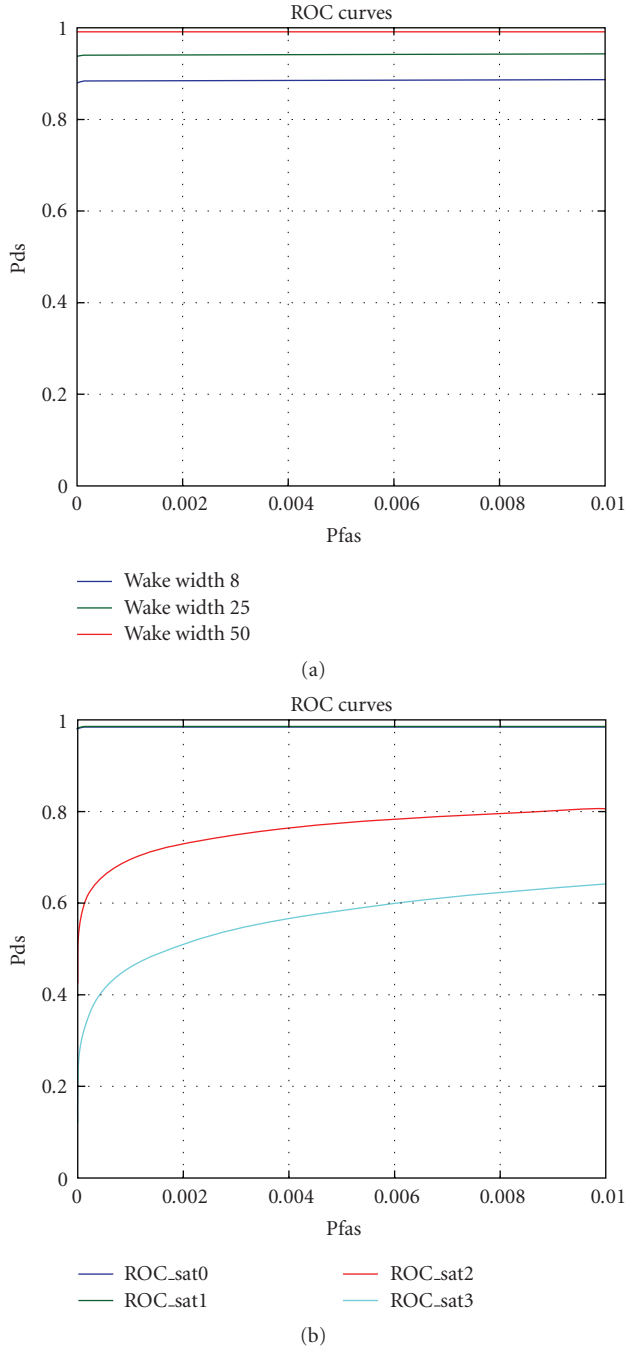
FIGURE 15: Evolution of sensor performance with (a) wake width and (b) satellite look angle (sat_0 = Nadir, sat_1 = 0.47 rad, sat_2 = 0.93 rad, and sat_3 = 1.4 rad from Nadir). Sea state is 5. Wake length is 2 km.

(the wake pdf is now located at the left of the open-sea pdf). Figure 16(b) compares detection performance during day ("−" curve) and night ("−." curve). Night detection performances are better. Indeed, it is well known that sun glint introduces false alarms.

Finally, we briefly examine performance obtained with the simulator when false alarms are present. We consider the presence of swells as a candidate for false alarms. Figure 17
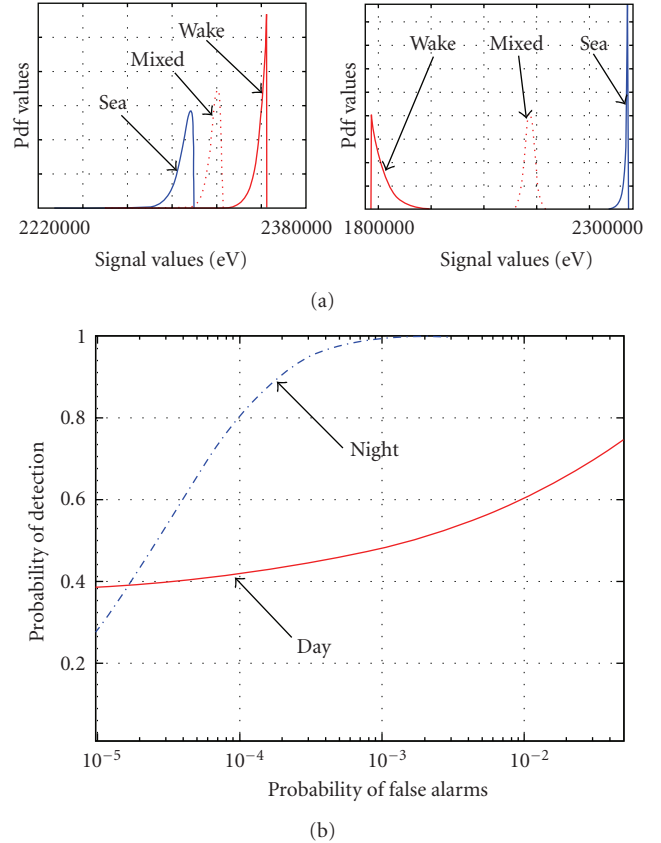

FIGURE 16: Sensor performance day versus night: (a) Wake, sea, and mixed pixel pdfs during the day (left) and the night (right) and (b) ROC curves before line detection. Sea state is 5. Wake length is 1 km.

TABLE 2: MTF budget at Nyquist and noise variances.

(a)

MTF at Nyquist	Value
Optical MTF	0.4
Detector MTF	0.64
Smearing MTF	0.82
Jitter MTF	0.9
Pointing MTF	0.9
Across-track MTF	0.21
Along-track MTF	0.17

(b)

Noise (eV)	Value
Photon	2007
Thermal	1107
Read out	420

compares ROC curves when the sea model contains gravity waves ("−" curve) and when both gravity waves and swells are present ("−." curve). As expected, performances with swells are degraded.
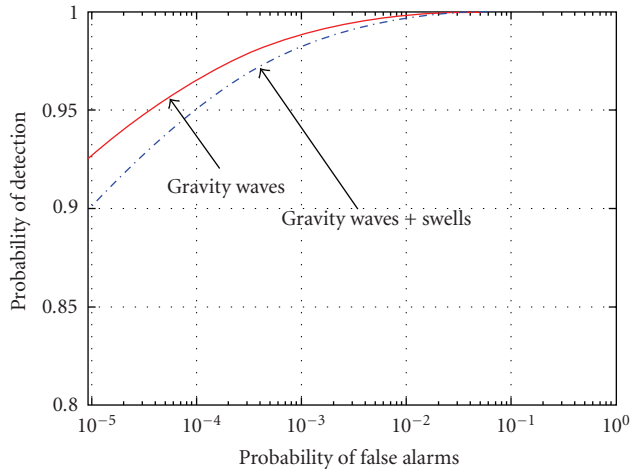
FIGURE 17: Sensor performance when the sea surface model includes (a) gravity waves and (b) gravity waves and swells after line detection. Sea state is 5. Wake length is 1 km.

9. Conclusions

This paper was devoted to the design of a real-time methodology for assessing detection performance of spaceborne sensors. Real-time capabilities are obtained by representing pixels in the images with random processes with given probability density functions. It was described in the case of mid-wave infrared (MWIR) sensors. However, its principles are applicable to any electro-optical sensor and even to radar sensors, provided that adequate models for the random processes are inserted into the model. Using this methodology to study sensor performance was then studied for a particular scenario.

Acknowledgment

References

[1] S. E. Lagaras and N. K. Uzunoglu, "A model for the passive infrared detection of naval targets through FLIR: model description and preliminary results applicable in the eastern Mediterranean Sea," *International Journal of Infrared and Millimeter Waves*, vol. 29, no. 6, pp. 596–607, 2008.

[2] C. Melsheimer, H. Lim, and C. Shen, "Observation and analysis of ship wakes in ERS-SAR and spot images," in *Proceedings of the 20th Asian Conference on Remote Sensing (ACRS '99)*, pp. 554–559, November 1999.

[3] J. P. Kerekes and J. E. Baum, "Spectral imaging system analytical model for subpixel object detection," *IEEE Transactions on Geoscience and Remote Sensing*, vol. 40, no. 5, pp. 1088–1101, 2002.

[4] J. Kerekes and J. Baum, "Fully-spectrum spectral imaging system analytical model," *IEEE Transaction on Geoscience and Remote Sensing*, vol. 43, no. 3, pp. 571–580, 2005.

[5] M. Bernhardt, M. I. Smith, P. G. Whitehead, L. N. Hunt, D. L. Hickman, and C. Dent II, "A statistical sea-surface clutter model in the long-wave infrared," in *Targets and Backgrounds X: Characterization and Representation*, W. R. Watkins, D. Clement, and W. R. Reynolds, Eds., vol. 5431 of *Proceedings of SPIE*, pp. 270–278, Orlando, Fla, USA, April 2004.

[6] C. Cochin, T. Landeau, G. Delhommeau, and B. Alessandrini, "Simulator of ocean scenes observes by polarimetric SAR," in *Proceedings of the 5th International Conference on Radar Systems*, pp. 17–21, Brest, France, May 1999.

[7] D. Crisp, "The state-of-the-art in ship detection in synthetic aperture radar imagery," Tech. Rep., DSTO Information Sciences Laboratory, Edinburgh, South Australia, 2004.

[8] I. Hennings, R. Romeiser, W. Alpers, and A. Viola, "Radar imaging of Kelvin arms of ship wakes," *International Journal of Remote Sensing*, vol. 20, no. 13, pp. 2519–2543, 1999.

[9] G. Zilman, A. Zapolski, and M. Marom, "The speed and beam of a ship from its wake's SAR images," *IEEE Transactions on Geoscience and Remote Sensing*, vol. 42, no. 10, pp. 2335–2343, 2004.

[10] A. Benilov, G. Bang, A. Safray, and I. Tkachenko, "Ship wake detectability in the ocean turbulent environment," in *Proceedings of the 23rd Symposium on Naval Hydrodynamics*, pp. 687–703, 2001.

[11] M. Barkat, *Signal Detection and Estimation*, Artech House, Boston, Mass, USA, 1991.

[12] F. Schwenger and E. Repasi, "Sea surface simulation for testing of multiband imaging sensors," in *Targets and Backgrounds IX: Characterization and Representation*, vol. 5075 of *Proceedings of SPIE*, pp. 72–84, Orlando, Fla, USA, April 2003.

[13] F. Schwenger and E. Repasi, "Sea surface simulation in the infrared modeling and validation," in *Targets and Backgrounds XII: Characterization and Representation*, vol. 6239 of *Proceedings of SPIE*, Orlando, Fla, USA, April 2006.

[14] M. K. Ochi, *Ocean Waves the Stochastic Approach*, Cambridge University Press, London, UK, 1998.

[15] R. A. Schowengerdt, *Remote Sensing: Models and Methods for Image Processing*, Academic Press Elsevier, San Diego, Calif, USA, 2007.

[16] R. Siegel and J. Howell, *Thermal Radiation Heat Transfer*, Hemisphere, Washington, DC, USA, 3rd edition, 1992.

[17] I. Wilf and Y. Manor, "Simulation of sea surface images in the infrared," *Applied Optics*, vol. 23, no. 18, pp. 3174–3180, 1984.

[18] J. Duffie and W. Beckman, *Solar Engineering of Thermal Processes*, John Wiley & Sons, New York, NY, USA, 1980.

[19] G. Walton, *Thermal Analysis Research Program*, U.S. Government, Washington, DC, USA, 1983.

[20] O. Corp, "The MODTRAN software," http://www.modtran.org/.

[21] M. Suh and K. Park, "A simple method for the cloud detection over land using daytime AVHRR data," in *Proceedings of the 18th Asian Conference on Remote Sensing*, Kuala Lumpur, Malaysia, October 1997.

[22] A. Benbouzid, K. Laidi, and A. Rachedi, "Hardware mask for cloud detection approach," in *Proceedings of the 2nd International Symposium on Communications, Control and Signal Processing (ISCCSP '06)*, Marrakech, Morocco, March 2006.

[23] C. Cox and W. Munk, "Measurement of the roughness of the sea surface from photographs of the sun's glitter," *Journal of the Optical Society of America*, vol. 44, no. 11, pp. 838–850, 1954.

[24] A. Daniels, *Field Guide to Infrared Systems*, SPIE Press, Bellingham, Wash, USA, 2007.

[25] NIST SEMATECH, *Engineering Statistics Handbook*, http://www.itl.nist.gov/div898/handbook/.

[26] R. D. Peltzer, W. D. Garrett, and P. M. Smith, "A remote sensing study of a surface ship wake," *International Journal of Remote Sensing*, vol. 8, no. 5, pp. 689–704, 1987.

[27] G. Du and T. S. Yeo, "A novel radon transform-based method for ship wake detection," in *Proceedings of the International Geoscience and Remote Sensing Symposium (IGARSS '04)*, vol. 5, pp. 3069–3072, September 2004.

[28] K. Raghupathy, *Curve tracing and curve detection in images*, M.S. thesis, Cornell University, Ithaca, NY, USA, 2004.